



Contents lists available at ScienceDirect

Materials Today Advances

journal homepage: www.journals.elsevier.com/materials-today-advances/

Enhanced thermoelectric performance in the zintl antimonides (Ca,RE)₉Cd₄Sb₉ (RE = rare-earth metal). Synergy between increased structural complexity and drive towards optimized chemical bonding

M.O. Ogunbunmi^{a,1}, S. Baranets^{a,b,1}, S. Bobev^{a,*}^a Department of Chemistry and Biochemistry, University of Delaware, Newark, DE, 19716, United States^b Department of Chemistry, Louisiana State University, Baton Rouge, LA, 70803, United States

ARTICLE INFO

Article history:

Received 6 September 2022

Received in revised form

5 October 2022

Accepted 10 October 2022

Available online xxx

Keywords:

Antimonides

Zintl Phases

Thermoelectrics

ABSTRACT

The interplay of structural complexity, high carrier mobility, and high density of states effective mass can play a pivotal role in achieving enhanced thermoelectric (TE) performance in candidate materials. In this regard, the Zintl phases represent a class of compounds that are susceptible to harboring these key ingredients. This, in addition to their amenability to various forms of chemical substitution mechanisms makes them a good choice of systems to explore systematically. Here we demonstrate the role-play of these ingredients in achieving excellent TE properties on single-crystals of $\text{Ca}_{9-x}\text{RE}_x\text{Cd}_{4+\delta}\text{Sb}_9$ (RE = Ce, Pr, Nd, Sm, Gd, Tb; $x \approx 0.5-0.8$, $y \approx 0.5-0.7$, $\delta \approx 0.25$). These phases represent a new addition to the “9–4–9” family with intricate chemical bonding arising from both a purposely introduced disorder on Ca sites and the inherent presence of interstitial Cd positions. Many of the newly synthesized and characterized phases show moderate values of the Seebeck coefficient, lying in the range of 71–116 $\mu\text{V/K}$ at 600 K and evolving as degenerate semiconductors. Simultaneously, the electrical resistivity $\rho(T)$ of the measured samples can be as low as 0.18 m Ω cm at this temperature. As a result, the observed TE power factors in the Ce-, Nd-, and Sm-samples are in the range 6–46 $\mu\text{W/cm.K}^2$. For $\text{Ca}_{9-x}\text{Ce}_x\text{Cd}_{4+\delta}\text{Sb}_9$, the estimated thermoelectric quality factor $B > 0.4$ at 300 K, which corresponds to a figure of merit $zT \geq 1$. Calculations based on the single parabolic band (SPB) model show that the optimum region for thermoelectric performance requires carrier concentration $n = 2-6 \times 10^{19} \text{ cm}^{-3}$ thus providing for an open window to further tune the TE properties.

© 2022 The Authors. Published by Elsevier Ltd. This is an open access article under the CC BY-NC-ND license (<http://creativecommons.org/licenses/by-nc-nd/4.0/>).

1. Introduction

The pnictides with the orthorhombic $\text{Ca}_9\text{Zn}_4\text{Bi}_9$ structure type [1], also broadly referred to as the “9–4–9” phases, have been extensively studied. They present a prototype material for studying the role of partially occupied interstitial position(s) to leverage greater electronic structure stability and means to fine-tune transport properties with major alterations of the average structure. Previous reports have already established the fact that this structure is best conceived as $A_9M_{4+x}Pn_9$ ($A = \text{Ca, Sr, Eu, Yb}$; $M = \text{Mn, Zn, Cd}$; $Pn = \text{pnictogen}$) [2–6] wherein the interstitial sites drive the stability of the structure and provides an electron count

that is reconcilable to the transport properties and electronic structure. Additional details on this aspect are provided in the crystal structure section (*vide infra*). It is also noted that the “9–4–9” phases are amenable to different substitution mechanisms as exemplified in $A_{9-x}\text{RE}_xM_4Pn_9$ [7] (RE = rare-earth metal), $A_9(M^{2+})_{4-x}(M^{3+})_xPn_9$ ($M^{3+} = \text{group 13 element}$) [5,8], and $A_9(M^{2+})_{4-x}(M^+)_{2+x-y}\square_yPn_9$ ($M^+ = \text{group 11 element}$; $\square = \text{defect}$) [9]. These substitutional variants clearly demonstrate the utility of the approach wherein the valence electron count being amended leads to naturally increased structural complexities and varying crystallographic symmetry.

Besides the interest in the “9–4–9” phases from fundamental research perspectives, much work in the area has been inspired from the point of view of materials applications geared towards the discovery and design of efficient thermoelectric materials. The structural characteristics of these phases can be conceived, in a very simplified form, as consisting of A^{2+} cations and polyanionic

* Corresponding author.

E-mail address: bobev@udel.edu (S. Bobev).¹ These authors contributed equally.

fragments made up of *M* and *Pn* atoms. This reflects the notion of them being Zintl phases, i.e., structure rationalization having to do with a bonding type that entails the transfer of electrons from the electropositive A^{2+} to the electronegative *Pn* atoms. Covalent bonds are formed in order to achieve closed-shell electronic configurations for all atoms. Following the Zintl-Klemm concept [10], as demonstrated in previous reports [7], these materials can be classified as Zintl phases which are known to feature narrow bandgaps that can promote high carrier mobility between the valence band to the conduction band. The narrow bandgap here is achieved in the degenerate state regime and can drive high electrical conductivity σ which is a key ingredient in achieving a high thermoelectric figure of merit $zT = S^2\sigma T/(\kappa_E + \kappa_L)$, where S , σ , κ_E and κ_L are the Seebeck coefficient, electrical conductivity, electronic thermal conductivity, and lattice thermal conductivity, respectively. Furthermore, the intricate bonding and interstitial sites domicile in these phases has been shown to promote low κ_L and enhance their thermoelectric performance [3,4,11,12]. For example, in $\text{Ca}_{9-x}\text{Eu}_y\text{Zn}_{4+\delta}\text{Sb}_9$ ($y \approx 2.25$ and $\delta \approx 0.7$), a substitution mechanism that considers an isoelectronic substitution of the Ca^{2+} site with Eu^{2+} was found to yield a low $\kappa_L \approx 0.25 \text{ W/m.K}$ and a $zT \approx 1.05$ at 773 K [12], thus paving way for more concerted efforts in the investigation of these phases for medium and high-temperature thermoelectric materials that can find applications either for solid-state cooling or heat conversion into electrical energy.

Motivated by these findings, we undertook studies aimed at the Ca-RE-Cd-Sb systems, where *RE* = rare-earth metal. From this work, six new materials emerged, with their unique structures being represented by the general formulae $\text{Ca}_{9-x}\text{RE}_y\text{Cd}_{4+\delta}\text{Sb}_9$ (*RE* = the early to mid-late rare-earths Ce, Pr, Nd, Sm, Gd, and Tb; $x \approx 0.5\text{--}0.8$, $y \approx 0.5\text{--}0.7$, $\delta \approx 0.25$). The present report outlines a new twist to the crystal chemistry of the “9–4–9” phases where the aliovalent substitutions of the Ca^{2+} cations with trivalent RE^{3+} ones, alongside the presence of a partial occupied Cd interstitial site, drive the structures to an extraordinary level of complexity. The induced disorder is expected to contribute to an ultra-low κ_L which together with a favorable σ can be beneficial for enhancing zT . It must also be noted that, up until now, a ternary $\text{Ca}_9\text{Cd}_{4+\delta}\text{Sb}_9$ phase or any of its substituted variants have not been successfully synthesized and characterized. Thus, the title phases are expected to provide additional understanding into the intricate bonding of the “9–4–9” phases, and may show potential to exhibit excellent thermoelectric properties.

2. Experimental section

2.1. Synthetic procedures

All elemental weighing and manipulations were carried out in an Ar-filled glovebox or under vacuum. Single crystals of $\text{Ca}_{9-x}\text{RE}_y\text{Cd}_{4+\delta}\text{Sb}_9$ (*RE* = Ce, Pr, Nd, Sm, Gd, Tb; $x \approx 0.5\text{--}0.8$, $y \approx 0.5\text{--}0.7$, $\delta \approx 0.25$) were synthesized through both solid-state direct reactions and high-temperature Cd self-flux reactions. Since the chemical formulae reflect complex structural disorder, they are complicated. To avoid verbosity throughout the text, hereafter, we will use simplified notation $(\text{Ca,RE})_9\text{Cd}_4\text{Sb}_9$.

Reactions with other rare-earth metals were also tried, but the observed structures for *RE* = La, Dy–Tm are not the same as those under consideration in this paper and will be reported elsewhere. The elements were used as purchased from Sigma-Aldrich and Alfa-Aesar with typical purity exceeding 99.9 wt% (metal basis). The start, Ca, *RE*, Cd, and Sb were weighed in the 8:1:4:9 stoichiometric ratio and loaded into Nb-tubes that was subsequently shut and transferred to an arc-welding chamber, where it was evacuated and sealed using Ar plasma. The sealed tubes were then transferred to

fused silica tubes, which were then evacuated, and flame-sealed under vacuum and loaded into tube furnaces. The temperature profile was: i) heating to 1298 K at the rate of 100 K h^{-1} ; ii) maintaining this temperature for 72 h; iii) quenching in cold water. The silica tubes were cracked, and the Nb-tubes transferred into the glovebox where they were opened. The products of these reactions were small crystal (micron sizes) of the $(\text{Ca,RE})_9\text{Cd}_4\text{Sb}_9$ phases, as identified by diffraction experiments.

The second approach for the synthesis relied on the Cd self-flux method. Here, elemental mixtures were weighed in the 8:1:60:9 (Ca:RE:Cd:Sb) molar ratio, respectively, and loaded into alumina crucibles that were further encased in fused silica ampoules packed between two balls of quartz wool. The ampoules were subsequently evacuated and flame-sealed under a vacuum and loaded in an upright manner into programmable muffle furnaces. The temperature profile was as follows: i) slowly heating from 373 K to 773 K at the rate of 60 K h^{-1} ; ii) maintaining this temperature for 6 h; iii) rapidly heating to 1323 K at the rate of 100 K h^{-1} ; iv) at this point, the reactions were allowed to proceed for 96 h, after which the temperature was then brought to 873 K at the rate of 4 K h^{-1} ; v) finally, the tubes were taken out of the furnaces and centrifuged at high speed to remove excess molten Cd. The tubes were subsequently taken to the Ar-filled glove box and the products extracted. The products of these reactions were mostly needle-like crystals (in the range of 1–3 mm) that show high metallic-luster appearance. By single-crystal X-ray diffraction, the crystals were confirmed to be the $(\text{Ca,RE})_9\text{Cd}_4\text{Sb}_9$ phases (before further use for property measurements).

CAUTION! Cd is highly toxic, and experiments related to this element must be handled with extreme care! The high vapor pressure of cadmium at the reaction temperature of 1323 K may cause the sealed silica tubes to break, which could lead to potentially hazardous conditions. Use of well-sealed and thick (1.5+ mm) silica tubes is necessary to reduce such risks.

2.2. Powder X-ray diffraction (PXRD)

Powder X-ray diffraction (PXRD) measurements were carried out at room temperature on a Rigaku Miniflex diffractometer (filtered Cu K α radiation, $\lambda = 1.5418 \text{ \AA}$), operated inside a nitrogen-filled glovebox. Small portions of the obtained single crystals were grounded into powder using agate mortars and pestles inside an argon-filled glove box. Data were collected between 5 and 75° in 2θ with a step size of 0.05° and 2 s per step counting time. The powder diffraction patterns for the samples were matched with the theoretically generated patterns (based on the single-crystal X-ray structural elucidation), which confirmed that the bulk of the phase is the target composition. PXRD measurements before and after exposure to air indicate that these phases are stable in air over a long period of up to 3 weeks.

2.3. Single-crystal X-ray diffraction (SCXRD)

Suitable single-crystals were selected in the glovebox and were cut under dry Paratone-N oil to appropriate dimensions ($\leq 0.10 \text{ mm}$). After that, crystals were scooped by MiTeGen plastic loops and transferred to the goniometer of a Bruker APEX II diffractometer, equipped with monochromatized Mo K α radiation, $\lambda = 0.71073 \text{ \AA}$. Data were collected under a stream of cold nitrogen at 200(2) K and then processed with SAINT and SADABS software packages implemented in the APEX3 program [13,14]. Crystal structures were solved by the intrinsic phasing method using SHELXT and refined by full-matrix least-squares methods on F^2 with SHELXL [15,16]. Despite the observed heavy disorder, no lower symmetry or evidence of superstructure that would allow to

resolve it (even partially) were found.

Atomic coordinates were standardized using the STRUCTURE TIDY program [17], but the atomic labels were set to be consistent with previously published data [7]. Selected details of the data collection and relevant crystallographic parameters are given in Tables 1 and 2 and Tables S1–S6 in the Supporting Information. CCDC 2202058–2202,063 contain the full supplementary crystallographic data for the compounds discussed in this paper. CIF files can be obtained free of charge via www.ccdc.cam.ac.uk/data_request/cif, or by emailing data_request@ccdc.cam.ac.uk, or by contacting The Cambridge Crystallographic Data Center, 12 Union Road, Cambridge CB2 1EZ, U.K., fax +44 1223 336033.

2.4. Transport properties measurements

All the measurements were carried out under high vacuum environment. Given the anisotropic crystal structure, we must note here that for needle-like crystals, the direction in which they grow fastest is expected to be the shortest crystallographic axis. In the present orthorhombic structure, this is the *c*-direction.

Seebeck coefficient *S* measurements were carried out using the integral method, and a constantan wire used as a reference on a SB-100 module MMR Tech. Instrument. The sample was mounted on the platform using a high-purity silver conductive paint and interfaced with the probe using the same silver conductive paint. Data were collected for temperatures between 300 and 600 K.

High-temperature resistivity measurements within a temperature window of 300–500 K using a H-50 module sourced from MMR Tech. Were carried out. Measurements were carried out using the four-probe Van der Pauw method on samples utilizing platinum wires with contacts made with high-purity silver paint. Similarly, the Hall coefficient measurements were carried out on the MMR Tech. Instrument using an applied magnetic field of 0.5 T.

Table 1

Selected Data Collection Details and Crystallographic Data for (Ca,*RE*)₉Cd₄Sb₉ (*RE* = Ce–Nd, Sm, Gd, Tb; *T* = 200(2) K; Mo *K*α, λ = 0.71073 Å; space group *Pbam*, *Z* = 2).

Chemical formula	Ca _{8.30(1)} Ce _{0.63(1)} Cd _{4.24(1)} Sb ₉	Ca _{8.35(1)} Pr _{0.59(1)} Cd _{4.28(1)} Sb ₉	Ca _{8.23(1)} Nd _{0.70(1)} Cd _{4.25(1)} Sb ₉
fw/ g mol ^{−1}	1992.70	1993.86	2003.71
<i>a</i> / Å	12.718(3)	12.684(4)	12.669(4)
<i>b</i> / Å	22.176(5)	22.192(7)	22.142(6)
<i>c</i> / Å	4.6345(9)	4.6293(14)	4.6295(14)
<i>V</i> / Å ³	1307.1	1303.1	1298.7
ρ _{calc} / g cm ^{−3}	5.06	5.08	5.12
μ(Mo– <i>K</i> α)/ cm ^{−1}	151.8	152.7	155.7
<i>R</i> ₁ (<i>I</i> > 2σ(<i>I</i>)) ^a	0.0255	0.0324	0.0315
<i>wR</i> ₂ (<i>I</i> > 2σ(<i>I</i>)) ^a	0.0434	0.0567	0.0532
<i>R</i> ₁ (all data) ^a	0.0325	0.0499	0.0427
<i>wR</i> ₂ (all data) ^a	0.0456	0.0629	0.0568
Δρ _{max,min} / e [−] ·Å ^{−3}	1.49, −1.47	1.55, −1.59	1.96, −1.79
CCDC code	2,202,058	2,202,059	2,202,060
Chemical formula	Ca _{8.41(1)} Sm _{0.55(1)} Cd _{4.23(1)} Sb ₉	Ca _{8.48(1)} Gd _{0.47(1)} Cd _{4.25(1)} Sb ₉	Ca _{8.52(1)} Tb _{0.46(1)} Cd _{4.25(1)} Sb ₉
fw/ g mol ^{−1}	1990.97	1988.58	1986.68
<i>a</i> / Å	12.670(3)	12.642(4)	12.646(2)
<i>b</i> / Å	22.175(5)	22.201(6)	22.178(4)
<i>c</i> / Å	4.6259(9)	4.6217(13)	4.6245(8)
<i>V</i> / Å ³	1299.7	1297.2	1297.0
ρ _{calc} / g cm ^{−3}	5.09	5.09	5.09
μ(Mo– <i>K</i> α)/ cm ^{−1}	154.3	154.6	154.9
<i>R</i> ₁ (<i>I</i> > 2σ(<i>I</i>)) ^a	0.0297	0.0288	0.0309
<i>wR</i> ₂ (<i>I</i> > 2σ(<i>I</i>)) ^a	0.0593	0.0535	0.0602
<i>R</i> ₁ (all data) ^a	0.0323	0.0360	0.0323
<i>wR</i> ₂ (all data) ^a	0.0605	0.0559	0.0610
Δρ _{max,min} / e [−] ·Å ^{−3}	2.48, −2.21	2.00, −1.57	2.39, −1.78
CCDC code	2,202,061	2,202,062	2,202,063

^a *R*₁ = ∑||*F*_o||−||*F*_c||/∑||*F*_o||; *wR*₂ = [∑(*w*(*F*_o²−*F*_c²)²)/∑(*w*(*F*_o²))] ^{1/2}, where *w* = 1/[σ(*F*_o²)+(AP)²+(BP)] and *P*=(*F*_o²+2*F*_c²)/3. *A* and *B* are the respective weight coefficients (see the CIF data).

Table 2

Refined atomic coordinates and equivalent isotropic displacement parameters (*U*_{eq}^a) for Ca_{8.30(1)}Ce_{0.63(1)}Cd_{4.24(1)}Sb₉.

Atom	Site	<i>X</i>	<i>Y</i>	<i>z</i>	<i>U</i> _{eq} / Å ²
Ca1	2a	0	0	0	0.019(1)
M2 ^b	4h	0.3616(1)	0.3555(1)	1/2	0.031(1)
M3 ^c	4h	0.0561(1)	0.4083(1)	1/2	0.021(1)
M4 ^c	4h	0.1248(1)	0.2340(1)	1/2	0.033(1)
Ca5	4g	0.2821(1)	0.0992(1)	0	0.021(1)
Cd1A ^d	4g	0.2233(1)	0.4521(1)	0	0.021(1)
Cd1B ^d	4g	0.3130(20)	0.4256(13)	0	0.021(1)
Cd2A ^d	4g	0.3830(1)	0.2569(1)	0	0.024(1)
Cd2B ^d	4g	0.4665(1)	0.2280(1)	0	0.024(1)
Cd3A ^e	4h	0.0249(11)	0.0762(6)	1/2	0.024(1)
Cd3B ^e	4h	0.1374(11)	0.1107(6)	1/2	0.024(1)
Cd3C ^b	4h	0.4612(14)	0.4037(10)	1/2	0.031(1)
Sb1	2c	0	1/2	0	0.017(1)
Sb2A ^d	4h	0.1845(1)	0.0060(3)	1/2	0.016(1)
Sb2B ^d	4h	0.1813(8)	0.9931(8)	1/2	0.016(1)
Sb3	4h	0.3701(1)	0.1869(1)	1/2	0.023(1)
Sb4	4g	0.0378(1)	0.1470(1)	0	0.015(1)
Sb5	4g	0.1845(1)	0.3280(1)	0	0.015(1)

^a *U*_{eq} is defined as one-third of the trace of the orthogonalized *U*_{ij} tensor.

^b M2 and Cd3C sites were refined with the following constraints: 1 = 0.779(4)Ca + 0.188(3)Ce + 0.0329(15)Cd.

^c Refined occupancies of the mixed-occupied Ca/Ce sites: M3 = 0.948(3)Ca + 0.052Ce; M4 = 0.924(3)Ca + 0.076Ce.

^d Positional disorder on Cd1, Cd2, and Sb2 sites was refined with the following site occupancies: 1 = 0.9822(12)Cd1A + 0.0178Cd1B, 1 = 0.6312(10)Cd2A + 0.3687Cd2B, 1 = 0.82(3)Sb2A + 0.18Sb2B.

^e Refined occupancy for the partially occupied sites: 0.0420(15)Cd3A and 0.0420(14)Cd3B.

2.5. Elemental microanalysis

Metallographic analyses were conducted on the various crystals to confirm their elemental compositions. Some single crystals were selected and mounted on a carbon tape glued to an aluminum

holder. The analyses were performed on Auriga 60 Cross Beam Scanning Electron Microscope equipped with Oxford Synergy X-MAX80 & EDSD (electron backscattering diffraction) X-ray energy-dispersive (EDX) spectrometer. The beam current was 10 μA at 20 kV accelerating potential. Data were collected over several spot and the observed stoichiometry in agreement with the single crystal X-ray diffraction structural elucidations shown in Table 1. The EDX result and SEM image for $\text{Ca}_{8.30(1)}\text{Ce}_{0.63(1)}\text{Cd}_{4.24(1)}\text{Sb}_9$ are shown in Figure S2.

3. Results and discussion

3.1. Synthesis

Here, we provide additional details on the synthesis of the reported phases. As earlier noted in the experimental section, the synthesis of these phases through the direct reaction method only produced small-sized crystals that cannot be used for physical measurements but were suitable for single-crystal X-ray diffraction. To overcome this limitation, we attempted the flux synthesis method and this technique too soon proved challenging in synthesizing the desired phase. Our first attempts involved Sn as a flux and started by loading the elements $\text{Ca}/\text{RE}/\text{Cd}/\text{Sb}/\text{Sn}$ in the molar ratio of 8:1:4:9:23, respectively. Heat treatment included increasing temperature to 773 K at the rate of 100 K h^{-1} and maintained for 6 h before heating to 1223 K at the rate of 100 K h^{-1} and homogenized for 96 h. The reaction was gradually cooled to 873 K at the rate of 4 K h^{-1} and quickly centrifuged at high speed to remove excess molten Sn. The products of these reactions were small crystals of the recently reported “10–1–1–9” phases [18,19], as well as some “14–1–11” crystals [20]. Few crystals from the “2–1–2” [21] family were also identified, but no presence of the targeted “9–4–9” phase. Other subsequent trials involved changes in the loading composition, for example $\text{Ca}:\text{RE}:\text{Cd}:\text{Sb}:\text{Sn}$ in the molar ratio of 8:1:12:9:70, respectively, as well as exploring various temperature profiles. The composition with extra Cd mainly produced the “2–1–2” phase, while diluting the mixture in more Sn yielded crystals of the “10–1–1–9” phase which were much larger in size. Switching Sn to Pb as a flux was tried, but the reactions did not produce the desired phases.

After many trials, we finally attempted the use of Cd flux in the synthesis of these phases. As noted in previous reports employing Cd flux synthesis [22–24], this approach can be a very powerful tool for accessing new inorganic materials. Our reactions with the starting elemental composition of $\text{Ca}:\text{RE}:\text{Cd}:\text{Sb}$ with the molar ratio of 8:1:60:9 was found to be suitable for the growth of the target phase. Here we further note that although the $(\text{Ca},\text{RE})_9\text{Cd}_4\text{Sb}_9$ could be successfully synthesized with this approach, the parent ternary $\text{Ca}_9\text{Cd}_4\text{Sb}_9$ phase could not be synthesized—instead, the experiments yielded a new noncentrosymmetric polymorph of the “2–1–2” phase [22]. One should also be reminded that a hypothetical compound $\text{Ca}_9\text{Cd}_{4+\delta}\text{Sb}_9$ ($\delta \approx 0.5$) is compositionally very similar to Ca_2CdSb_2 , which likely explains the inability to synthesize the former. We must also state that while exploring the chemistry of the “2–1–2” phase, it was observed that RE substitution on the Ca sites can only be observed for the heavy rare-earth Lu (at minute levels, i.e., $\text{Ca}_{1.98}\text{Lu}_{0.02}\text{CdSb}_2$). For the lighter RE atoms, such experiments appeared to favor the “9–4–9” phase, as reported herein. In addition, one of our reactions involving Tb was noted to also produce the “2–1–2” phase which can likely be attributed to the fact that the RE substitution with Ca for heavy RE elements favors the “2–1–2” phase while those of the lighter RE elements favors the “9–4–9” phase.

3.2. Crystal structure, chemical bonding, and structural relationships

Structural complexity is an inherent feature of the Zintl pnictides within the “9–4–9” family. It originates from the electron-deficient nature of the archetype phase, which can be rationalized within the fully ionic approximation as follows: $(\text{Ca}^{2+})_9(\text{M}^{2+})_4(\text{Sb}^{3-})_9(h^+)$, where $M = \text{Mn}, \text{Zn}, \text{Cd}$; and h^+ stands for hole. While an initial structural study performed by Schäfer more than 40 years ago indicated the absence of structural disorder [1], an accurate investigation confirmed the presence of a partially occupied M site, resulting in the charge-balanced composition $(\text{Ca}^{2+})_9(\text{M}^{2+})_{4.5}(\text{Sb}^{3-})_9$ [2,25]. The interstitial M site is in a distorted tetrahedral, or rather, pyramidal coordination by three Sb atoms (Fig. 1a). Such a coordination environment is not atypical for Zintl phases with d^9 and d^{10} elements, and the pyramidalization (i.e., deviation from trigonal-planar geometry) is usually less pronounced for Zn than for Cd [26,27].

A different mechanism for achieving a charge-balanced composition can be the substitution of Ca with rare-earth metals. The reported $(\text{Ca},\text{RE})_9\text{Cd}_4\text{Sb}_9$ phases are new examples of such aliovalent substituted compounds within the Ca–Cd–Sb system, adding to the “14–1–11” [23], and “11–1–9” [18,28] families of phases. This approach has also been implemented for the series $\text{Ca}_{9-x}\text{RE}_x\text{Mn}_4\text{Sb}_9$ ($\text{RE} = \text{La}–\text{Nd}, \text{Sm}$; $x \approx 1$), where trivalent lanthanides randomly substitute divalent Ca atoms in the structure, making the quaternary phases to be narrow-gap semiconductors according to the formula $(\text{Ca}^{2+})_8(\text{RE}^{3+})_1(\text{Mn}^{2+})_4(\text{Sb}^{3-})_9$ [7]. One should notice that there is no interstitial partially occupied Mn site in the latter structures (Fig. 2).

Both $\text{Ca}_9\text{Mn}_4\text{Pn}_9$ and $\text{Ca}_{9-x}\text{RE}_x\text{Mn}_4\text{Sb}_9$ phases exhibit noticeable structural differences with regard to the way the corner-sharing $[\text{MnPn}_4]$ tetrahedra ($\text{Pn} = \text{Sb}, \text{Bi}$) are packed in space (Fig. 2). While the anionic substructure of the former can be described as disorder-free $[\text{Mn}_4\text{Pn}_9]$ 1D-ribbons of corner-sharing $[\text{MnPn}_4]$ tetrahedra (Fig. 1a), the anionic substructure of the latter is complemented by the split position in the proximity to Mn2 site (Fig. 1b). Such structural fragments are also observed in the crystal structures of $(\text{Ca},\text{RE})_9\text{Cd}_4\text{Sb}_9$, for which a more detailed structural description will be provided in the following paragraphs.

All compositions presented here with the general formula $(\text{Ca},\text{RE})_9\text{Cd}_4\text{Sb}_9$ ($\text{RE} = \text{Ce}, \text{Pr}, \text{Nd}, \text{Sm}, \text{Gd}, \text{and Tb}$) are isostructural and crystallize in the orthorhombic crystal system with the space group $Pbam$ (no. 55) with two formula units per unit cell, akin to the $\text{Ca}_9\text{Mn}_4\text{Bi}_9$ archetype [1]. As noted earlier, the “9–4–9” chemistry could be extended to include other lanthanides, but the structures of $\text{Ca}_{9-x}\text{RE}_x\text{Cd}_{4+\delta}\text{Sb}_9$ ($\text{RE} = \text{La}, \text{Dy}–\text{Tm}$) are different and will be a subject of a forthcoming publication. The basic unit is the same though and its structural description can be found elsewhere [1,2,5–9,25,29]. Here, we will focus our attention on the subtleties of the $\text{Ca}_{9-x}\text{RE}_x\text{Cd}_{4+\delta}\text{Sb}_9$ crystal structure, which contains a total of 18 crystallographic sites in the asymmetric unit, in contrast to the 12 sites in $\text{Ca}_9\text{Mn}_4\text{Bi}_9$ or 13 sites in the $\text{Ca}_{9-x}\text{RE}_x\text{Mn}_4\text{Sb}_9$. The “extra” sites are all partially occupied, indicating a noticeable degree of disorder (Fig. 2c).

Indeed, among the five typical sites for the Sb atoms, the Sb2 position in all refined $(\text{Ca},\text{RE})_9\text{Cd}_4\text{Sb}_9$ structures exhibits positional disorder and is split into two sites—Sb2A and Sb2B—with an approximate ratio of 82(3):18% (Table 2, Tables S1–S5 check). The origin of such disorder is likely related to the presence of two interstitial partially occupied Cd sites, Cd3A and Cd3B. This is a noteworthy difference between the structures of $\text{Ca}_{9-x}\text{RE}_x\text{Cd}_{4+\delta}\text{Sb}_9$ and $\text{Ca}_{9-x}\text{RE}_x\text{Mn}_4\text{Sb}_9$, with the latter being much less disordered (Fig. 1b) [7]. In particular, each pair of two split sites (Cd1A and

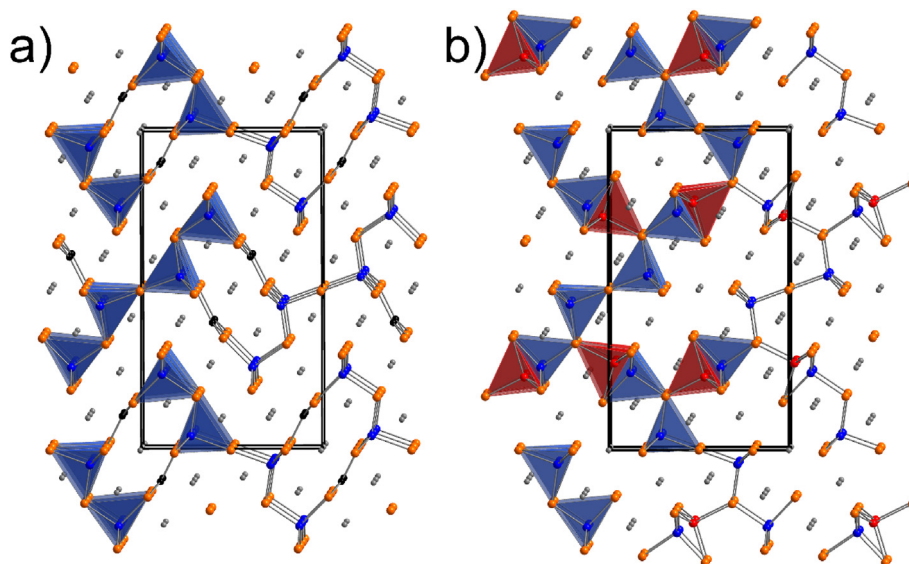


Fig. 1. Crystal structure of the $A_9M_{4+\delta}Pn_9$ family of compounds ($A = \text{Ca, Sr, Eu, Yb}$; $M = \text{Mn, Zn, Cd}$; $Pn = \text{Sb, Bi}$) (a) and $\text{Ca}_{9-x}\text{RE}_x\text{Mn}_4\text{Sb}_9$ ($\text{RE} = \text{La-Nd, Sm}$; $x \approx 1$) series (b) in the combined polyhedral and ball-and-stick representation. The AE^{2+} cations, M atoms, and Pn atoms are drawn as dark grey, blue, and orange spheres, respectively. The interstitial partially occupied $M3$ atoms in $A_9M_{4+\delta}Pn_9$ are shown as black spheres. The supplementary split $M2$ position in $\text{Ca}_{9-x}\text{RE}_x\text{Mn}_4\text{Sb}_9$ is drawn as red spheres. Unit cells are outlined in black.

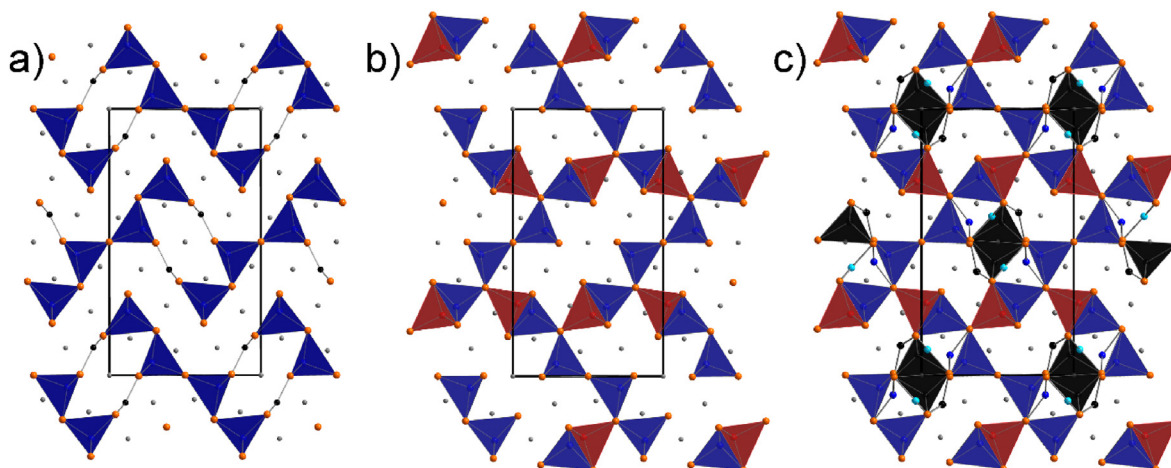


Fig. 2. Schematic representation of the three “9–4–9” polymorphs: $\text{Ca}_9\text{Zn}_{4+\delta}\text{Sb}_9$ (a), $\text{Ca}_{9-x}\text{RE}_x\text{Mn}_4\text{Sb}_9$ (b), and the title $\text{Ca}_{9-x}\text{RE}_x\text{Cd}_{4+\delta}\text{Sb}_9$ (c). Ca and Ca/RE atoms are shown in grey, $M1$ and $M2$ sites are shown in blue, complementary split $M2$ site is shown in red, interstitial Zn3 site in $\text{Ca}_9\text{Zn}_{4+\delta}\text{Sb}_9$ and Cd3A/Cd3B sites in $\text{Ca}_{9-x}\text{RE}_x\text{Cd}_{4+\delta}\text{Sb}_9$ are shown in black. Interstitial Cd3C site is shown in sky-blue. The coloring of the coordination polyhedra matches the color of central atoms. Notice that all Cd sites in (c) are partially occupied.

Cd2B , Cd2A and Cd2B , Cd3A and Cd3B) form two face-sharing Cd -centered polyhedra (Fig. 3), with either tetrahedral or nearly trigonal planar geometry. Interatomic distance between each pair of split Cd atoms is in the range 1.24–1.62 Å, which is much lower than the doubled covalent radius of Cd (1.44 Å) [30]. Such geometrical restriction is resolved by the simultaneous structural refinement of both split sites with a total occupancy of 100% (for Cd1 and Cd2) or less (for Cd3A and Cd3B).

The split on the Cd1 site is minuscule, yet, consistent for the entire reported series, with a significant dominance of the Cd1A site (97–98%) over Cd1B (Table 2, Tables S1–S5). Atomic coordinates of Cd1A site are identical to those for the Cd1 site in the rest of reported “9–4–9” phases (Fig. 2) [7]. A coordination environment of Cd1A position resembles a distorted tetrahedron formed by two Sb2 (either Sb2A or Sb2B), Sb5 , and Sb1 atoms (Fig. 3a). A Cd1A-Sb1 interatomic distance slightly exceeds 3 Å yet can be considered as a bonding interaction. Cd1B site is trigonally

coordinated by three Sb atoms, namely Sb2 and Sb5 , while the fourth contact of 3.28 Å is significantly longer than the sum of the covalent radii of Cd and Sb (2.83 Å) [30]; this interaction is depicted with a dashed line in Fig. 3a and is arguably very weakly bonding.

The split of the Cd2 position into Cd2A and Cd2B sites resembles the case of $\text{Ca}_{9-x}\text{RE}_x\text{Mn}_4\text{Sb}_9$ (Fig. 2) [7]. Akin to the latter, a slight increase of Cd2A site dominance is observed across the series, with the occupancies of Cd2A and Cd2B in a ratio of ca. 2:1 for the Ce and Pr samples; the ratio changes to ca. 3:1 for the Gd and Tb samples (Table 2 and S1–S5. N.B. Cd2 and Cd2B correspond to Mn2 and Mn3 sites in the previous report) [7]. We explained this trend in the previous report [7] by a combination of geometric factors coupled with electrostatic considerations originated from Ca/RE substitution. Both Cd2A and Cd2B sites tetrahedrally coordinated by two Sb3 atoms, Sb4 , and Sb5 atoms with Cd-Sb distances in the range 2.79–3.04 Å (Fig. 3b).

While there is no interstitial Mn site in the $\text{Ca}_{9-x}\text{RE}_x\text{Mn}_4\text{Sb}_9$

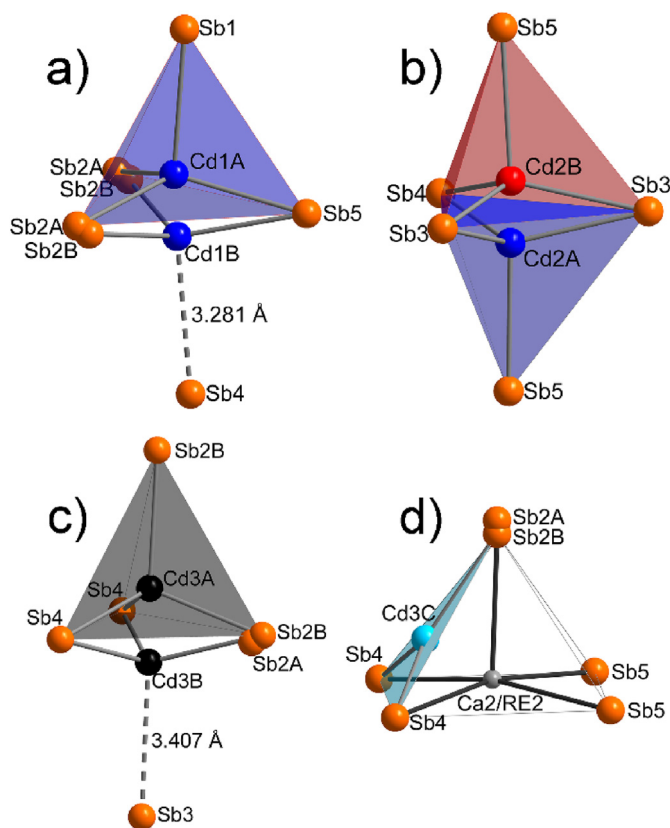


Fig. 3. Close-up view of the coordination environment and disorder of Cd1 (a), Cd2 (b), Cd3 (c) sites. The distorted tetrahedral coordination is observed for Cd1A, Cd2A, Cd2B, and Cd3A atoms. Trigonal-planar coordination environment for Cd3C atom (d) is presented in conjunction with square-pyramidal coordination of Ca2/RE2 site. The color code is the same as in Fig. 2.

series of compounds, Cd3 site was observed for all members of the title quaternary series. As we already mentioned, the presence of partially occupied M3 site in $A_9M_{4+x}Pn_9$ ($AE = Ca, Sr, Eu, Yb$; $M = Mn, Zn, Cd$; $Pn = Sb, Bi$) family of compounds is favorable from electronic reasons and helps to maintain the charge balance [2,6,25,29]. The site occupancy factors (SOFs) for this site vary in a wide range from ca. 3% in $Ca_9Cd_{4.06}Bi_9^{29}$ to ca. 24% in $Ca_9Zn_{4.48}Sb_9$ [2]. Akin to the other two sites, Cd3 site also undergoes a split into Cd3A and Cd3B with relatively low freely refined SOFs in the range 3.5%–6.3% (Table 2 and S1–S5, Fig. 3c). Noteworthy, the atomic coordinates for Cd3B site correspond to the interstitial site in the parent $A_9M_{4+x}Pn_9$ (Fig. 2). This site is trigonally coordinated by Sb3B and two Sb4 atoms with distances in the range 2.62–2.76 Å. Coordination environment of Cd3A site resembles a distorted tetrahedron formed by two Sb4 atoms and two Sb2B atoms with Cd–Sb interatomic distances falling in the range of 2.67–3.04 Å (Table S6). Short Cd–Sb contacts are the result of the partial occupancy of Cd sites, as observed before in other Zintl phases [26]. All refined Cd–Sb bond lengths are in good agreement with the expected covalent bonding character of the interactions.

Another important point of the discussion is the aliovalent substitution of trivalent rare-earth ions on Ca^{2+} sites. According to the structure refinements (Table 1), the rare-earth metal content exhibits a slightly decreasing trend across the series, although there is some non-uniformity. The exact opposite trend was observed for the $Ca_{9-x}RE_xMn_4Sb_9$ series, where rare-earth metal content per formula unit is increasing across the series [7]. The reasons for the opposite behavior of the Cd- and Mn-based specimens are unclear

and we can only speculate that the root-cause is the “extra” content of Cd.

Only three out of five Ca sites, Ca2, Ca3, and Ca4 exhibited a considerable degree of “overoccupancy” when their site occupation factors were freely refined. Therefore, Ca2, Ca3, and Ca4 were modelled as mixed occupied Ca/RE sites. A local coordination environment of all Ca and Ca/RE sites is presented in Figure S1. Among them, Ca2/RE2 site requires a special attention. First, a non-negligible residual electron density peak was observed 1.65 Å away from the Ca2/RE2 site, which indicated the presence of additional, partially occupied site. This interstitial position is located almost in the center of the triangle formed by Sb2 and two Sb4 atoms (Fig. 3d), with approximate distances of 2.73(2) Å to Sb4 and 2.70(3) Å to Sb2B. The stated bond lengths and the trigonal coordination is unusual for Ca atom, but suitable for Cd [26]. The new site was assigned as Cd3C and its SOF was refined simultaneously with the Ca2/RE2 position to avoid the structural model with simultaneous existence of both sites (Table 2). This structural feature is responsible for the complicated notation of $Ca_{9-x}RE_yCd_{4+y}Sb_9$ with different x and y values. Similar type of disorder was recently reported for $A_{10}MSb_9$ ($A = Ca, Yb$; $M = Mn, Zn, Ga, In$) [31,32], where two cationic sites, A with octahedral coordination and M with tetrahedral coordination, were jointly refined. We can also refer to another related scenario, wherein the incorporation of Cu and Ag into the structure of $Eu_9Cd_4Sb_9$ induced a disorder on Cd sites, which required a model with a tetrahedral and a nearly trigonal planar atomic site to be refined together [9,11].

Another observation related to the above-mentioned disorder on the Ca2/RE2 site pertains to the noticeable elongation of the thermal ellipsoids oriented along the imaginary axis drawn between Sb2 and Sb3 (Figure S1). Such elongation becomes more evident for structures with the heavier lanthanides, requiring additional split of the Ca2/RE2 site was for the Sm-, Gd-, and Tb-bearing phases. Obviously, both split sites must be considered a mixture of Ca and rare-earth metal, yet, handling of such structural model becomes too complicated, especially given the proximity of Cd3C. Therefore, we modelled the disorder as a major site assigned to Ca and the minor site assigned to the rare-earth metal (Figure S1). Although such model may affect the precision of the refined composition, it is not expected that the resultant deviation from the actual chemical make-up will be significant.

The discussed structural features help to understand the structure-properties relationships in the title compounds. The latter represent unique examples in which the concentration of charge-carriers is simultaneously controlled via two independent factors: i) the occupancy of the interstitial Cd sites, and ii) the degree of rare-earth metal substitutions. The reason for such complex behavior might be the ability of the Cd atoms to become trigonally coordinated and may play a crucial role. For instance, such reduced coordination environment is not typical for Mn, which may explain why typical single-doping mechanism was observed for the $Ca_{9-x}RE_xMn_4Sb_9$ series. A pronounced stability of the trigonal planar coordination of Zn allows us to suggest a similar double-doping mechanism for yet to be developed $(Ca,RE)_9Zn_4Sb_9$ series.

3.3. Electron counting considerations and transport properties

Following the comprehensive structural discussions, we can now reconcile the heavy disorder with the drive (from an electronic structure standpoint) of the structure to achieve an optimal valence electron count. Taking $Ca_{8.30(1)}Ce_{0.63(1)}Cd_{4.24(1)}Sb_9$ as an example $(Ca,RE)_9Cd_4Sb_9$ composition, it is easy to see that there are just enough number of electrons to classify this composition as a Zintl phase—the electrons can be partitioned on the basis of the Zintl-Klemm rules as follows: $(Ca^{2+})_{8.30}(Ce^{3+})_{0.63}(Cd^{2+})_{4.24}$

(Sb^{3-}) $_9(\text{h}^+)$ $_{0.03}$, where h^+ stands for holes. The present formula shows that the composition can be considered as almost completely charge-balanced: i.e., as a Zintl phase. The rest of the refined compositions are also close to being charge-balanced. The non-zero h^+ value is indicative of a likely p-type semiconducting behavior, which is experimentally confirmed (*vide infra*). One may notice that the charge balance for the Pr- and Nd-bearing samples indicate a small concentration of electrons as charge carriers. We discuss the likely impact of this further in the transport properties section (*vide infra*). Although it is also worth mentioning that calculated content of electrons/holes in the formula unit is within 3σ , therefore these numbers must be considered carefully.

Plots of the electrical resistivity $\rho(T)$ of $(\text{Ca},\text{RE})_9\text{Cd}_4\text{Sb}_9$ single crystals are presented in Fig. 4. $\rho(T)$ of $(\text{Ca},\text{Ce})_9\text{Cd}_4\text{Sb}_9$ and $(\text{Ca},\text{Sm})_9\text{Cd}_4\text{Sb}_9$ are low and reminiscent of those of metals. The magnitude of $\rho(T)$ at 300 K in both phases are 0.12 and 0.51 m Ω cm which corresponds to a significantly large electrical conductivity ($\sigma = 1/\rho$). The $(\text{Ca},\text{Nd})_9\text{Cd}_4\text{Sb}_9$ and $(\text{Ca},\text{Gd})_9\text{Cd}_4\text{Sb}_9$ phases also feature a noticeably low $\rho(T)$ of the order of 6.6 and 25.2 m Ω cm, respectively at 300 K. However, the observed magnitude of $\rho(T)$ for the $(\text{Ca},\text{Pr})_9\text{Cd}_4\text{Sb}_9$ phase is relatively higher than those of the other four phases which hints at the possibly low carrier concentration in this phase. We discuss this aspect further in the later part of this section.

Also, it is important to compare the observed values here to those reported for some related phases. For example, in $\text{Ca}_{9-x}\text{RE}_x\text{Mn}_4\text{Sb}_9$ phases [7], $\rho(T)$ values of ca. 66 m Ω cm, 220 m Ω cm, and 65 m Ω cm are reported for $\text{RE} = \text{Ce}$, Pr, Nd,

respectively at 300 K. In $\text{Ca}_{9-x}\text{Eu}_x\text{Zn}_{4.7}\text{Sb}_9$ ($x = 2.25$) [12], an electrical conductivity σ of ca. 3.75×10^4 S/m is observed at 300 K, which corresponds to 2.67 m Ω cm while values of ~ 1 m Ω cm, 5000 m Ω cm, and 8850 m Ω cm, all at 300 K, have also been reported for $\text{Ca}_9(\text{Zn}_{1-x}\text{In}_x)_4\text{Sb}_9$ [8], $\text{Eu}_9\text{Mn}_{2.87}\text{Al}_{1.13}\text{Sb}_9$ [5] and $\text{Yb}_9\text{Mn}_{3.59}\text{Al}_{0.41}\text{Sb}_9$ [5], respectively. From the varied magnitudes of $\rho(T)$, it is evident that the values can range from as low as ~ 1 m Ω cm to a significantly high magnitude of 8850 m Ω cm, which are attributed to the roles of the carrier concentration of interstitial atoms which can significantly affect the carrier mobility. Another important aspect of the “9–4–9” phases is their inherent narrow bandgaps which fall in the range of ~ 0.01 – 0.2 eV [5,7,8]. Such an observation is ubiquitous in Zintl phases and can be an indication of the realization of a closed shell electronic configuration [33]. It is also noted that such feature can result in a relatively high electrical conductivity that is driven by high carrier mobility [34]. Although the bandgaps in the reported phases are not immediately available, but it is expected that the various values will also fall into the observed range. This notion is even more plausible considering the temperature evolution of ρ in the title phases, which mostly feature degenerate semiconducting behavior. From the Hall coefficient measurements on the various samples at 300 K, the Hall carrier concentration n_H and Hall mobility μ_H are $(\text{Ca},\text{Ce})_9\text{Cd}_4\text{Sb}_9$: $1.88 \times 10^{20} \text{ cm}^{-3}$ and $312.84 \text{ cm}^2/\text{V.s}$, $(\text{Ca},\text{Pr})_9\text{Cd}_4\text{Sb}_9$: $8.82 \times 10^{17} \text{ cm}^{-3}$ and $32.5 \text{ cm}^2/\text{V.s}$, $(\text{Ca},\text{Nd})_9\text{Cd}_4\text{Sb}_9$: $1.46 \times 10^{20} \text{ cm}^{-3}$ and $11.68 \text{ cm}^2/\text{V.s}$, $(\text{Ca},\text{Sm})_9\text{Cd}_4\text{Sb}_9$: $2.04 \times 10^{20} \text{ cm}^{-3}$ and $44.04 \text{ cm}^2/\text{V.s}$, $(\text{Ca},\text{Gd})_9\text{Cd}_4\text{Sb}_9$: $1.54 \times 10^{19} \text{ cm}^{-3}$ and $8.78 \text{ cm}^2/\text{V.s}$, respectively. Here the observed n_H and μ_H provide us with additional intuition into the nature of the transport properties in the title phases and agree with the magnitudes of ρ .

The temperature dependence of Seebeck coefficient $S(T)$ for $(\text{Ca},\text{RE})_9\text{Cd}_4\text{Sb}_9$ single crystals are presented in Fig. 5. The $(\text{Ca},\text{Sm})_9\text{Cd}_4\text{Sb}_9$ phase features the lowest $S(T) = 44.5 \mu\text{V/K}$ at room temperature and which gradually increases to $\sim 70.7 \mu\text{V/K}$ at 600 K. This relatively small S agrees with the small magnitude of ρ

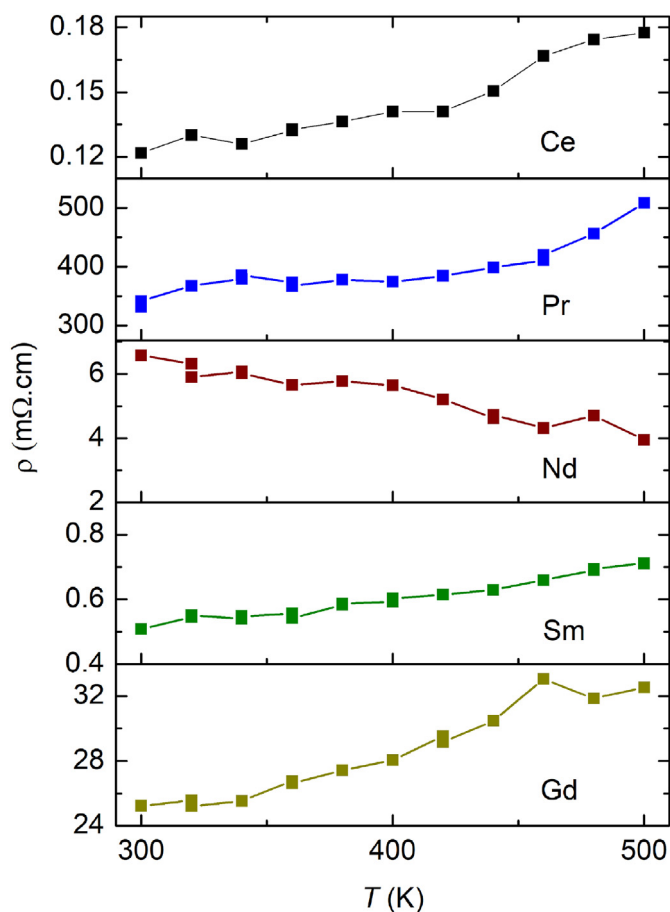


Fig. 4. Temperature dependence of electrical resistivity $\rho(T)$ of $(\text{Ca},\text{RE})_9\text{Cd}_4\text{Sb}_9$ ($\text{RE} = \text{Ce}$, Pr, Nd, Sm, Gd).

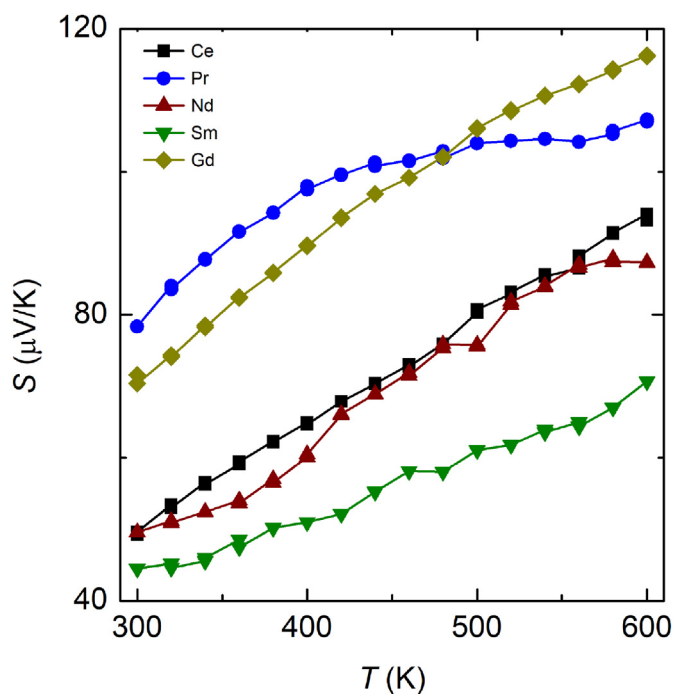


Fig. 5. Temperature dependence of Seebeck coefficient $S(T)$ of $(\text{Ca},\text{RE})_9\text{Cd}_4\text{Sb}_9$ ($\text{RE} = \text{Ce}$, Pr, Nd, Sm, Gd).

observed. $S(T)$ of $(\text{Ca,Ce})_9\text{Cd}_4\text{Sb}_9$ and $(\text{Ca,Nd})_9\text{Cd}_4\text{Sb}_9$ achieve nearly the same value of ca. 49.6 $\mu\text{V/K}$ at 300 K and increases with comparable slope to 600 K with magnitudes of 94.1 and 87.4 $\mu\text{V/K}$, respectively.

The $(\text{Ca,Gd})_9\text{Cd}_4\text{Sb}_9$ phase attains a magnitude of 71.6 $\mu\text{V/K}$ and gradually increases to 116.3 $\mu\text{V/K}$, while the $(\text{Ca,Pr})_9\text{Cd}_4\text{Sb}_9$ phase appears to have the highest room temperature value of 78.4 $\mu\text{V/K}$ which gradually increases upon heating until about 440 K, where a weak temperature dependence of $S(T)$ sets in. In this regard, although the room temperature magnitude of $(\text{Ca,Pr})_9\text{Cd}_4\text{Sb}_9$ is higher than that of $(\text{Ca,Gd})_9\text{Cd}_4\text{Sb}_9$, the magnitude of $(\text{Ca,Pr})_9\text{Cd}_4\text{Sb}_9$ ca. 107 $\mu\text{V/K}$ lags that of $(\text{Ca,Gd})_9\text{Cd}_4\text{Sb}_9$ at 600 K. The observation in $(\text{Ca,Pr})_9\text{Cd}_4\text{Sb}_9$ is consistent with its high $\rho(T)$ value and the weak temperature behavior at intermediate temperature likely signifies the excitation of minority carriers in what can be associated with a bipolar effect. A closer look at the data of $(\text{Ca,Nd})_9\text{Cd}_4\text{Sb}_9$ above 560 K also reflects this effect. Coincidentally, it turns out that the simple charge-balance based on the refined compositions of these two phases, $(\text{Ca}^{2+})_{8.35}(\text{Pr}^{3+})_{0.59}(\text{Cd}^{2+})_{4.28}(\text{Sb}^{3-})_9(\text{e}^-)_{0.03}$ and $(\text{Ca}^{2+})_{8.23}(\text{Nd}^{3+})_{0.7}(\text{Cd}^{2+})_{4.25}(\text{Sb}^{3-})_9(\text{e}^-)_{0.06}$, reveal a slight surplus of electrons, comparison to those of other phases which are rather slightly electron-deficient. It is therefore likely that such composition drives the bipolar conduction effects as observed in both phases. Furthermore, within the degenerate limit, S can be written as [35]:

$$S = \frac{2k_B T}{3e h^2} \left(\frac{\pi}{3n} \right)^{\frac{2}{3}} m^* (r + 1) \quad (1)$$

where e , k_B , h , m^* , n , and r are the electron charge, the Boltzmann constant, the reduced Planck constant, the (density of state) effective mass, the carrier concentration, and the scattering parameter, respectively. The above expression indicates that for a degenerate semiconductor, S is expected to vary directly with m^* and inversely with n . Based on the Single Parabolic Band (SPB) model, the value of m^* can be estimated from the experimental values of $S(T)$ presented in Fig. 5. We discuss this aspect further in the later part of this section.

Fig. 6a shows the plots of the thermoelectric power factor $PF (= S^2/\rho)$ of the reported phases. Here the significantly high $\rho(T)$ and the feature of bipolar effect in $(\text{Ca,Pr})_9\text{Cd}_4\text{Sb}_9$ in $S(T)$ manifests in the significantly low $PF \sim 0.02 \mu\text{W/cm.K}^2$. The PF of $(\text{Ca,Gd})_9\text{Cd}_4\text{Sb}_9$ varies from ~ 0.2 to $0.37 \mu\text{W/cm.K}^2$ while that of $(\text{Ca,Nd})_9\text{Cd}_4\text{Sb}_9$ varies from 3.7 to $5.6 \mu\text{W/cm.K}^2$ between 300 and 600 K, respectively. In the $(\text{Ca,Sm})_9\text{Cd}_4\text{Sb}_9$ phase, PF varies from ~ 4 to $6.3 \mu\text{W}$

cm.K^2 between 300 and 600 K. It is noted here that the PF of Nd- and Sm-phases at 600 K are comparable. From these samples, $(\text{Ca,Ce})_9\text{Cd}_4\text{Sb}_9$ exhibits the highest PF that ranges from $\sim 19.89 \mu\text{W/cm.K}^2$ at 300 K to $45.17 \mu\text{W/cm.K}^2$ at 600 K. The observation in this phase can largely be attributed to the low and metallic-like $\rho(T)$ which translates into very high electrical conductivity and the $(\text{Ca,Ce})_9\text{Cd}_4\text{Sb}_9$ phase thus represents another example of a material where the role of heavy doping produces low metallic-type resistivity.

We present a variation of PF as a function of carrier concentration n at room temperature in Fig. 6b based on SPB model. The observation from $PF(n)$ here conveys an idea of the three phases namely $(\text{Ca,Ce})_9\text{Cd}_4\text{Sb}_9$, $(\text{Ca,Nd})_9\text{Cd}_4\text{Sb}_9$, and $(\text{Ca,Sm})_9\text{Cd}_4\text{Sb}_9$ being over doped. The optimum n here based on our calculations appears to fall in the region of $\sim 10^{19} \text{ cm}^{-3}$ which is an order of magnitude lower than the measured values. The observation here is also similar to the that in a recent report on $\text{Ca}_{10}\text{RECdSb}_9$ phases [19] where although, the optimum PF falls in a range of about an order of magnitude lower than the experimentally observed value. In this case, proper materials optimization is thus required to maximize the thermoelectric performance of these phases. Also shown in Fig. 6b are the effective masses m^* of these phases (0.67–0.8 m_e) which are comparable and within the same order of magnitude. But considering the relatively high magnitude of S observed in these phases at 600 K, m^* is expected to increase and it is likely to reflect a much heavier mass. The thermoelectric properties of these phases can further be examined by determining their weighted mobility μ_w which is given as:

$$\mu_w = \mu_H \left(\frac{m^* T/K}{m_e 300} \right)^{3/2} \quad (2)$$

Here μ_H is the Hall mobility and all terms have their usual meaning. Based on this expression, the calculated μ_w are 358.01, 6.61, and $76.70 \text{ cm}^2/\text{V.s}$, for $(\text{Ca,Ce})_9\text{Cd}_4\text{Sb}_9$, $(\text{Ca,Nd})_9\text{Cd}_4\text{Sb}_9$, and $(\text{Ca,Sm})_9\text{Cd}_4\text{Sb}_9$, respectively, at 300 K. The determined μ_w here can be conceptualized as the electron mobility weighted by the density of electronic state and it is especially useful here since it is independent of doping and can be used to directly probe the electronic band structure and the thermoelectric performance of these phases. The value of $358.01 \text{ cm}^2/\text{V.s}$ in $(\text{Ca,Ce})_9\text{Cd}_4\text{Sb}_9$ is comparable to that of $362 \text{ cm}^2/\text{V.s}$ in $\text{Yb}_{0.3}\text{Co}_4\text{Sb}_{12}$ [36] and $400 \text{ cm}^2/\text{V.s}$ in Bi_2Te_3 [37,38] which are well known for their remarkable thermoelectric properties. A similar comparison can be made too about the other two phases ($(\text{Ca,Nd})_9\text{Cd}_4\text{Sb}_9$ and $(\text{Ca,Sm})_9\text{Cd}_4\text{Sb}_9$) with magnitudes of about $8 \text{ cm}^2/\text{V.s}$ in Mg_3Sb_2 [39] and $83 \text{ cm}^2/\text{V.s}$ in CoSb_3 [36], respectively. The observed properties here are intriguing and may be a pointer to the excellent thermoelectric performance of these materials when properly tuned. As we conclude our discussions on the title phases, we turn our attention to another powerful parameter that can be invaluable to understanding the potential of these materials. The thermoelectric quality factor B is defined as:

$$B = \left(\frac{k_B}{e} \right)^2 \frac{8\pi e (2m_e k_B T)^{3/2}}{3h^3} \frac{\mu_w T}{K_L} = 4.33 \times 10^{-10} \frac{\mu_w T^5}{\mu_L} \quad (3)$$

where k_B , h , e , and κ_L represent Boltzmann's constant, Planck constant, electronic charge, and lattice thermal conductivity, respectively. It is immediately clear from this expression that $B \propto \mu_w/\kappa_L$, such that μ_w carries the same importance as κ_L and as such increasing the magnitude of μ_w is as important as achieving an ultra-low κ_L . Hence it is the combined effect of these two parameters that achieves an enhanced thermoelectric figure of merit zT . In this context, we can also estimate the magnitude of B at 300 K using the results from Eqn. (2). In the various reported “9–4–9” phases,

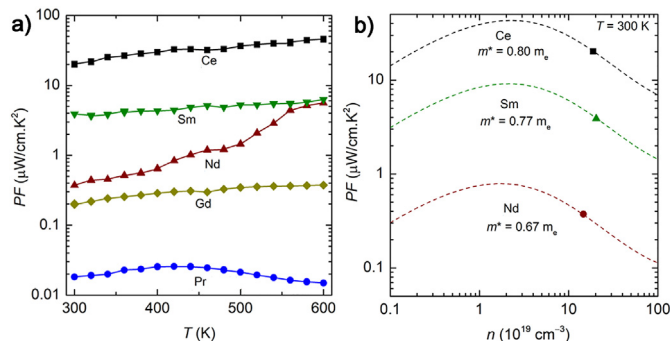


Fig. 6. (a) Temperature dependence of thermoelectric power factor $PF(T)$ of $(\text{Ca,RE})_9\text{Cd}_4\text{Sb}_9$ ($\text{RE} = \text{Ce, Pr, Nd, Sm, Gd}$). (b) Variation of PF with the carrier concentration of $(\text{Ca,Ce})_9\text{Cd}_4\text{Sb}_9$, $(\text{Ca,Nd})_9\text{Cd}_4\text{Sb}_9$, and $(\text{Ca,Sm})_9\text{Cd}_4\text{Sb}_9$ at 300 K based on SPB model is shown as dashed lines. The effective mass obtained for each of the phases are shown in various symbols.

the magnitudes of κ_L reported mainly fall in the range of 0.25–0.56 W/m.K [4,12,40,41] as such, the magnitude of B from Eqn. (3) at 300 K for these phases would be in the range of 0.43–0.97, 0.01–0.02, and 0.09–0.21 for $(\text{Ca,Ce})_9\text{Cd}_4\text{Sb}_9$, $(\text{Ca,Nd})_9\text{Cd}_4\text{Sb}_9$, and $(\text{Ca,Sm})_9\text{Cd}_4\text{Sb}_9$, respectively, and are much higher than those of several notable thermoelectric materials. Table 1 in reference no. [38] provides good comparisons with other well-known phases [38]. B here provides for the highest achievable zT of an optimally doped material and as well provide a useful toolbox to engineering their bandgap towards optimum efficiency. In the present case, only $(\text{Ca,Ce})_9\text{Cd}_4\text{Sb}_9$ presents a $B > 0.4$, as required for achieving a $zT \geq 1$ and the upper limit of $B \approx 0.97$ in this phase would generally correspond to a $zT \approx 2$ at this temperature.

4. Conclusions

The successful synthesis of the $(\text{Ca,RE})_9\text{Cd}_4\text{Sb}_9$ Zintl phases have been reported here, along with their structural elucidation. They represent yet another new structural modification of the “9–4–9” phase, and the preliminary assessment of their thermoelectric properties show a great promise. Thus, the $(\text{Ca,RE})_9\text{Cd}_4\text{Sb}_9$ family presents a test field to applicability as energy conversion materials.

A noteworthy structural feature reported here is the coexistence of two mechanisms for structural modifications, previously manifested only separately in $\text{AgM}_{4+\delta}\text{Pn}_9$ and $\text{Ag}_{9-x}\text{RE}_x\text{M}_4\text{Pn}_9$, where “ x ” and “ δ ” are independent tuning parameters. For $\text{Ca}_{9-x}\text{RE}_x\text{Cd}_{4+\delta}\text{Sb}_9$, they are interrelated and the structures therefore feature greater complexity that can drive an ultra-low κ_L . The transport properties on these phases indicate that they are doped p-type semiconductors. The calculated PF for these phases varies from as low as 0.02 $\mu\text{W}/\text{cm.K}^2$ in $(\text{Ca,Pr})_9\text{Cd}_4\text{Sb}_9$ to 45 $\mu\text{W}/\text{cm.K}^2$ in $(\text{Ca,Ce})_9\text{Cd}_4\text{Sb}_9$. The low magnitude of PF in $(\text{Ca,Pr})_9\text{Cd}_4\text{Sb}_9$ can be attributed to the presence of bipolar effect as well as a high value ρ of $\sim 500 \text{ m}\Omega \text{ cm}$ at 600 K. In this report, the properties of $(\text{Ca,Ce})_9\text{Cd}_4\text{Sb}_9$, $(\text{Ca,Nd})_9\text{Cd}_4\text{Sb}_9$, and $(\text{Ca,Sm})_9\text{Cd}_4\text{Sb}_9$ are particularly highlighted as they present a more promising opportunity for achieving enhanced thermoelectric performance. Calculation based on SPB show that the optimum PF in these phases lies in the region of $2\text{--}6 \times 10^{19} \text{ cm}^{-3}$. The result from the SPB model along with that of the calculated weighted mobility μ_w and thermoelectric quality factor B which generally compares with those of notable thermoelectric materials would therefore be invaluable in the band engineering and the optimization procedures of these phases.

Author Contributions

Michael O. Ogunbunmi: Investigation, Methodology, Formal analysis, Visualization, Writing – original draft.; Sviatoslav Baranets: Conceptualization, Investigation, Formal analysis, Writing – review & editing.; Svilen Bobev: Conceptualization, Supervision, Project administration, Writing – review & editing.

Funding sources

The authors acknowledge financial support from the United States Department of Energy, Office of Science, Basic Energy Sciences, under Award #DE-SC0008885.

Declaration of competing interest

The authors declare that they have no known competing financial interests or personal relationships that could have appeared to influence the work reported in this paper.

Data availability

CCDC 2202058–2202,063 contain the full supplementary crystallographic data for the compounds discussed in this paper. CIF files can be obtained free of charge via www.ccdc.cam.ac.uk/data_request/cif.

Acknowledgment

The authors are indebted to Dr. Stanislav Stoyko and Mr. Leonard Voss for carrying out early synthetic work in the Ca-RE-Cd-Sb systems.

Appendix A. Supplementary data

Supplementary data to this article can be found online at <https://doi.org/10.1016/j.mtadv.2022.100310>.

References

- [1] E. Brechtel, G. Cordier, H. Schäfer, Darstellung und kristallstruktur von $\text{Ca}_9\text{Mn}_4\text{Bi}_9$ und $\text{Ca}_9\text{Zn}_4\text{Bi}_9$ /preparation and crystal structure of $\text{Ca}_9\text{Mn}_4\text{Bi}_9$ and $\text{Ca}_9\text{Zn}_4\text{Bi}_9$, Z. Naturforsch. B Chem. Sci. 34 (9) (1979) 1229–1233, <https://doi.org/10.1515/znb-1979-0912>.
- [2] S. Bobev, J.D. Thompson, J.L. Sarrao, M.M. Olmstead, H. Hope, S.M. Kauzlarich, Probing the limits of the Zintl concept: structure and bonding in rare-earth and alkaline-earth zinc-antimonides $\text{Yb}_9\text{Zn}_{4+x}\text{Sb}_9$ and $\text{Ca}_9\text{Zn}_{4.5}\text{Sb}_9$, Inorg. Chem. 43 (16) (2004) 5044–5052, <https://doi.org/10.1021/ic049836j>.
- [3] Z. Wu, J. Li, X. Li, M. Zhu, K. Wu, X. Tao, B.-B. Huang, S.-Q. Xia, Tuning the thermoelectric properties of $\text{Ca}_9\text{Zn}_{4+x}\text{Sb}_9$ by controlled doping on the interstitial structure, Chem. Mater. 28 (19) (2016) 6917–6924, <https://doi.org/10.1021/acs.chemmater.6b02498>.
- [4] J. Zhang, Q. Liu, K.-F. Liu, W.-J. Tan, X.-C. Liu, S.-Q. Xia, $\text{Sr}_9\text{Mg}_{4.45(1)}\text{Bi}_9$ and $\text{Sr}_9\text{Mg}_{4.42(1)}\text{Sb}_9$: Mg-containing Zintl phases with low thermal conductivity, Inorg. Chem. 60 (6) (2021) 4026–4033, <https://doi.org/10.1021/acs.inorgchem.1c00078>.
- [5] X.-C. Liu, K.-F. Liu, Q.-Q. Wang, Y.-M. Wang, M.-Y. Pan, S.-Q. Xia, Exploring new Zintl phases in the 9–4–9 family via Al substitution. Synthesis, structure, and physical properties of $\text{Ae}_9\text{Mn}_{4-x}\text{Al}_x\text{Sb}_9$ (ae = Ca, Yb, Eu), Inorg. Chem. 56 (6) (2020) 3709–3717, <https://doi.org/10.1021/acs.inorgchem.9b03320>.
- [6] X.-C. Liu, Z. Wu, S.-Q. Xia, X.-T. Tao, S. Bobev, Structural variability versus structural flexibility. A case study of $\text{Eu}_9\text{Cd}_{4+x}\text{Sb}_9$ and $\text{Ca}_9\text{Mn}_{4+x}\text{Sb}_9$ ($x \approx 1/2$), Inorg. Chem. 54 (3) (2015) 947–955, <https://doi.org/10.1021/ic5023505>.
- [7] Y. Wang, S. Bobev, Rare-earth metal substitutions in $\text{Ca}_{9-x}\text{RE}_x\text{Mn}_4\text{Sb}_9$ (RE = La–Nd, Sm; $x \approx 1$). Synthesis and characterization of a new series of narrow-gap semiconductors, Chem. Mater. 30 (10) (2018) 3518–3527, <https://doi.org/10.1021/acs.chemmater.8b01316>.
- [8] D.M. Smiadak, S. Baranets, M. Rylko, M. Marshall, M. Calderón-Cueva, S. Bobev, A. Zevailink, Single crystal growth and characterization of new Zintl phase $\text{Ca}_9\text{Zn}_{3.1}\text{In}_{0.9}\text{Sb}_9$, J. Solid State Chem. 296 (2021), 121947, <https://doi.org/10.1016/j.jssc.2020.121947>.
- [9] N. Kazem, A. Hurtado, B. Klobes, R.P. Hermann, S.M. Kauzlarich, $\text{Eu}_9\text{Cd}_{4-x}\text{CM}_{2+x-y}\square_y\text{Sb}_9$: $\text{Ca}_9\text{Mn}_4\text{Bi}_9$ -type structure stuffed with coinage metals (Cu, Ag, and Au) and the challenges with classical valence theory in describing these possible Zintl phases, Inorg. Chem. 54 (3) (2015) 850–859, <https://doi.org/10.1021/ic502061w>.
- [10] R. Nesper, The zintl-klemm concept – a historical survey, Z. Anorg. Allg. Chem. 640 (14) (2014) 2639–2648, <https://doi.org/10.1002/zaac.201400403>.
- [11] N. Kazem, J.V. Zaikina, S. Ohno, G.J. Snyder, S.M. Kauzlarich, Coinage-metal-stuffed $\text{Eu}_9\text{Cd}_4\text{Sb}_9$: metallic compounds with anomalous low thermal conductivities, Chem. Mater. 27 (21) (2015) 7508–7519, <https://doi.org/10.1021/acs.chemmater.5b03808>.
- [12] C. Chen, W. Xue, X. Li, Y. Lan, Z. Zhang, X. Wang, F. Zhang, H. Yao, S. Li, J. Sui, P. Han, X. Liu, F. Cao, Y. Wang, Q. Zhang, Enhanced thermoelectric performance of Zintl phase $\text{Ca}_9\text{Zn}_{4+x}\text{Sb}_9$ by beneficial disorder on the selective cationic site, ACS Appl. Mater. Interfaces 11 (41) (2019) 37741–37747, <https://doi.org/10.1021/acsami.9b12748>.
- [13] Bruker AXS Inc, SAINT. Madison, Wisconsin, USA, 2014a.
- [14] Bruker AXS Inc, SADABS. Madison, Wisconsin, USA, 2014b.
- [15] G.M. Sheldrick, IUCr. SHELXT – integrated space-group and crystal-structure determination, Acta Crystallogr. Sect. A Found. Adv. 71 (1) (2015) 3–8, <https://doi.org/10.1107/S2053273314026370>.
- [16] G.M. Sheldrick, Crystal structure refinement with SHELXL, Acta Crystallogr. Sect. C Struct. Chem. 71 (2015) 3–8, <https://doi.org/10.1107/S2053229614024218>.
- [17] L.M. Gelato, E. Parthé, Structure TIDY – a computer program to standardize crystal structure data, J. Appl. Crystallogr. 20 (2) (1987) 139–143, <https://doi.org/10.1107/S0021889887086965>.
- [18] M.O. Ogunbunmi, S. Bobev, The highly disordered Zintl phase $\text{Ca}_{10}\text{GdCdSb}_9$ –

- new example of a *p*-type semiconductor with remarkable thermoelectric properties, *Mater. Today Phys.* 26 (2022), 100725, <https://doi.org/10.1016/j.mtphys.2022.100725>.
- [19] M.O. Ogunbunmi, S. Bobev, Observation of anomalously high Seebeck coefficients in the family of Zintl phase semiconductors $\text{Ca}_{10}\text{RECdSb}_9$ ($\text{RE} = \text{rare-earth metal}$), *Chem. Mater.* (2022), <https://doi.org/10.1021/acs.chemmater.2c02103>.
- [20] S. Baranets, L. Voss, S. Stoyko, S. Bobev, Synthesis, crystal structure and physical properties of the solid solutions $\text{Ca}_{14-x}\text{RE}_x\text{CdSb}_{11}$ ($\text{RE} = \text{La-Nd, Sm, Gd-Yb}$, $x \approx 0.85 \pm 0.15$), *J. Appl. Phys.* 125 (24) (2019), 245101, <https://doi.org/10.1063/1.5099632>.
- [21] S.-Q. Xia, S. Bobev, Cation–Anion interactions as structure directing factors: structure and bonding of Ca_2CdSb_2 and Yb_2CdSb_2 , *J. Am. Chem. Soc.* 129 (13) (2007) 4049–4057, <https://doi.org/10.1021/ja069261k>.
- [22] M.O. Ogunbunmi, S. Baranets, S. Bobev, Structural complexity and tuned thermoelectric properties of a polymorph of the Zintl phase Ca_2CdSb_2 with a non-centrosymmetric monoclinic structure, *Inorg. Chem.* 61 (28) (2022) 10888–10897, <https://doi.org/10.1021/acs.inorgchem.2c01354>.
- [23] S.-Q. Xia, S. Bobev, $\text{Ba}_{11}\text{Cd}_8\text{Bi}_{14}$: bismuth zigzag chains in a ternary alkaline-earth transition-metal Zintl phase, *Inorg. Chem.* 45 (18) (2006) 7126–7132, <https://doi.org/10.1021/ic060583>.
- [24] W. Peng, S. Baranets, S. Bobev, Synthesis, crystal and electronic structure of $\text{BaLi}_x\text{Cd}_{13-x}$ ($x \approx 2$), *Front. Chem. - Inorg. Chem.* (2022), <https://doi.org/10.3389/fchem.2022.991625>.
- [25] S.-Q. Xia, S. Bobev, New manganese-bearing antimonides and bismuthides with complex structures. Synthesis, structural characterization, and electronic properties of $\text{Yb}_9\text{Mn}_{4+x}\text{Pn}_9$ ($\text{Pn} = \text{Sb or Bi}$), *Chem. Mater.* 22 (3) (2010) 840–850, <https://doi.org/10.1021/cm901633r>.
- [26] S. Baranets, A. Ovchinnikov, S. Bobev, Structural diversity of the Zintl pnictides with rare-earth metals, in: *Handbook on the Physics and Chemistry of Rare Earths*, 2021, pp. 227–324, <https://doi.org/10.1016/bs.hpcr.2021.07.001>.
- [27] S. Baranets, A. Balvanz, M. Darone, G. S. Bobev, On the effects of aliovalent substitutions in thermoelectric Zintl pnictides. Varied polyanionic dimensionality and complex structural transformations – the case of Sr_3ZnP_3 vs $\text{Sr}_3\text{Al}_x\text{Zn}_{1-x}\text{P}_3$, *Chem. Mater.* 34 (9) (2022) 4172–4185, <https://doi.org/10.1021/acs.chemmater.2c00527>.
- [28] J. Wang, S.-Q. Xia, X.-T. Tao, $\text{A}_{10}\text{LaCdSb}_9$ ($\text{A} = \text{Ca, Yb}$): a highly complex Zintl system and the thermoelectric properties, *Chem. Asian J.* 8 (1) (2013) 251–257, <https://doi.org/10.1002/asia.201200827>.
- [29] S.-Q. Xia, S. Bobev, Interplay between size and electronic effects in determining the homogeneity range of the $\text{A}_9\text{Zn}_{4+x}\text{Pn}_9$ and $\text{A}_9\text{Cd}_{4+x}\text{Pn}_9$ phases ($0 \leq x \leq 0.5$), $\text{A} = \text{Ca, Sr, Yb}$, *J. Am. Chem. Soc.* 129 (32) (2007) 10011–10018, <https://doi.org/10.1021/ja0728425>.
- [30] B. Cordero, V. Gómez, A.E. Platero-Prats, M. Revés, J. Echeverría, E. Cremades, F. Barragán, S. Alvarez, Covalent radii revisited, *Dalton Trans.* (2008) 2832–2838, <https://doi.org/10.1039/b801115j>.
- [31] A. Ovchinnikov, S. Chanakian, A. Zevalkink, S. Bobev, Ultralow thermal conductivity and high thermopower in a new family of Zintl antimonides $\text{Ca}_{10}\text{MSb}_9$ ($\text{M} = \text{Ga, In, Mn, Zn}$) with complex structures and heavy disorder, *Chem. Mater.* 33 (9) (2021) 3172–3186, <https://doi.org/10.1021/acs.chemmater.0c04940>.
- [32] S. Baranets, A. Ovchinnikov, S. Bobev, Complex structural disorder in the Zintl phases $\text{Yb}_{10}\text{MnSb}_9$ and $\text{Yb}_{21}\text{Mn}_4\text{Sb}_{18}$, *Inorg. Chem.* 60 (9) (2021) 6702–6711, <https://doi.org/10.1021/acs.inorgchem.1c00519>.
- [33] M.O. Ogunbunmi, S. Baranets, A.B. Childs, S. Bobev, The Zintl phases Aln_2As_2 ($\text{A} = \text{Ca, Sr, Ba}$): new topological insulators and thermoelectric material candidates, *Dalton Trans.* 50 (26) (2021) 9173–9184, <https://doi.org/10.1039/D1DT01521D>.
- [34] M.O. Ogunbunmi, S. Baranets, S. Bobev, Synthesis and transport properties of the family of Zintl phases Ca_3RESb_3 ($\text{RE} = \text{La-Nd, Sm, Gd-Tm, Lu}$): exploring the roles of crystallographic disorder and core *4f* electrons for enhancing thermoelectric performance, *Chem. Mater.* 33 (23) (2021) 9382–9392, <https://doi.org/10.1021/acs.chemmater.1c03300>.
- [35] Y.I. Ravich, B.A. Efimova, I.A. Smirnov, in: L.S. Stil'bans (Ed.), *Semiconducting Lead Chalcogenides*, Springer US, Boston, MA, 1970, <https://doi.org/10.1007/978-1-4684-8607-0>.
- [36] Y. Tang, Z.M. Gibbs, L.A. Agapito, G. Li, H.-S. Kim, M.B. Nardelli, S. Curtarolo, G.J. Snyder, Convergence of multi-valley bands as the electronic origin of high thermoelectric performance in CoSb_3 skutterudites, *Nat. Mater.* 14 (12) (2015) 1223–1228, <https://doi.org/10.1038/nmat4430>.
- [37] T. Plecháček, J. Navrátil, J. Horák, P. Lošťák, Defect structure of Pb-doped Bi_2Te_3 single crystals, *Philos. Mag. A* 84 (21) (2004) 2217–2228, <https://doi.org/10.1080/14786430410001678226>.
- [38] I.T. Witting, T.C. Chasapis, F. Ricci, M. Peters, N.A. Heinz, G. Hautier, G.J. Snyder, The thermoelectric properties of bismuth telluride, *Adv. Electron. Mater.* 5 (6) (2019), 1800904, <https://doi.org/10.1002/aelm.201800904>.
- [39] K. Imasato, S.D. Kang, S. Ohno, G.J. Snyder, Band engineering in Mg_3Sb_2 by alloying with Mg_3Bi_2 for enhanced thermoelectric performance, *Mater. Horiz.* 5 (1) (2018) 59–64, <https://doi.org/10.1039/C7MH00865A>.
- [40] S. Ohno, U. Aydemir, M. Amsler, J.-H. Pöhl, S. Chanakian, A. Zevalkink, M.A. White, S.K. Bux, C. Wolverton, G.J. Snyder, Achieving $\text{ZT} > 1$ in inexpensive Zintl phase $\text{Ca}_9\text{Zn}_{4+x}\text{Sb}_9$ by phase boundary mapping, *Adv. Funct. Mater.* 27 (20) (2017), 1606361, <https://doi.org/10.1002/adfm.201606361>.
- [41] S.K. Bux, A. Zevalkink, O. Janka, D. Uhl, S. Kauzlarich, G.J. Snyder, J.-P. Fleurial, Glass-like lattice thermal conductivity and high thermoelectric efficiency in $\text{Yb}_9\text{Mn}_{4.2}\text{Sb}_9$, *J. Mater. Chem.* 2 (1) (2014) 215–220, <https://doi.org/10.1039/C3TA14021K>.